Journal of Atmospheric and Oceanic Technology
July 2013, Volume 30, Issue 7, Pages 1511-1526
http://dx.doi.org/10.1175/JTECH-D-12-00156.1

Exploring the Benefits of Using *CryoSat-2*'s Cross-Track Interferometry to Improve the Resolution of Multisatellite Mesoscale Fields

G. Dibarboure[a, *], P. Y. Le Traon[b], N. Galin[c]

[a] CLS, Ramonville St-Agne, France
[b] IFREMER, Plouzané, France
[c] Centre for Polar Observation and Modelling, Department of Earth Sciences, University College London, London, United Kingdom

*: Corresponding author : Gerald Dibarboure, email address : gerald.dibarboure@cls.fr

Abstract:

Sea surface height (SSH) measurements provided by pulse-limited radar altimeters are one-dimensional profiles along the satellite's nadir track, with no information whatsoever in the cross-track direction. The anisotropy of resulting SSH profiles is the most limiting factor of mesoscale SSH maps that merge the 1D profiles.

This paper explores the potential of the cross-track slope derived from the *Cryosphere Satellite-2* (*CryoSat-2*)'s synthetic aperture radar interferometry (SARin) mode to increase the resolution of mesoscale fields in the cross-track direction. Through idealized 1D simulations, this study shows that it is possible to exploit the dual SARin measurement (cross-track slope and SSH profile) in order to constrain mesoscale mapping in the cross-track direction.

An error-free SSH slope allows a single SARin instrument to recover almost as much SSH variance as two coordinated altimeters. Noise-corrupted slopes can also be exploited to improve the mapping, and a breakthrough is observed for SARin errors ranging from 1 to 5 *µ*rad for 150-km-radius features in strong currents, and 0.1–0.5 *µ*rad for global mesoscale.

Although only limited experiments might be possible with the error level of current *CryoSat-2* data, this paper shows the potential of the SAR interferometry technology to reduce the anisotropy of altimeter measurements if the SARin error is significantly reduced in the future, and in particular in the context of a prospective SARin demonstrator optimized for oceanography.

Keywords: Altimetry, Remote sensing, Sampling, Satellite observations, Interpolation schemes, Inverse methods

1. Introduction and context

In contrast with wide-swath imagers (e.g., sea surface temperature or ocean color), the data record of radar altimeters is exceedingly anisotropic. Sea surface height (SSH) measurements from pulse-limited radar altimeters are one-dimensional profiles along the satellite's nadir track, with no SSH information whatsoever in the cross-track direction. Figure 1 shows that, for a single altimeter flying on the TOPEX/Jason orbit, the along-track (white segment) resolution can be as small as 7 km (level 2 product, 1 Hz rate), whereas in the cross-track resolution (black segment) it can be as large as 300 km.

To reconstruct 2D gridded fields of SSH or sea level anomalies (SLA), it is therefore necessary to interpolate 1D profiles (e.g. AVISO 2010; Dibarboure et al, 2011a, Leben et al 2002, 2011). Optimal interpolation (OI) exploits an a priori statistical knowledge of the SLA field characteristics (e.g. Jacobs et al 2001; Le Traon et al, 2003) and measurement error (e.g. Philipps et al, 2012) as an additional constraint to merge 1D profiles from multiple sensors in an optimal way (e.g. Ducet, et al 2000).

The anisotropy of SSH profiles is by far the most limiting factor of gridded SSH mesoscale fields (Le Traon & Dibarboure, 2002, 2004; Pascual et al 2006), and especially in near real time where measurements "from the map's future" are not yet available (Pascual et al, 2008). There are two practical consequences to this limitation.

Firstly, even if the spatial and temporal scales used to constrain the OI are derived from SSH measurement of 2 to 4 satellite constellations, the mapping is limited in the cross-track direction. Because 1D profiles from multiple sensors are blended into one map, 2D mesoscale mapping uses a compromise between actual mesoscale correlations and the sampling limitations from such constellations (Ducet, et al, 2000).

The resolution of mesoscale fields is dominated by the number of altimeters in operation. Chelton & Schlax (2003), Le Traon & Dibarboure (2002), and Chelton et al (2011) have shown that mesoscale maps have a limited global resolution capability. Higher resolution can still be achieved, but only locally, at certain times, when enough 1D profiles are available (Dussurget et al, 2011).

In this context, a new technology used on CryoSat-2 has the unprecedented potential to add actual measurements to constrain mesoscale mapping in the *cross-track* direction. Indeed, in addition to a classical pulse-limited radar altimeter measurement (also known as low resolution mode or LRM), CryoSat-2's altimeter SIRAL features a synthetic aperture radar interferometry (SARin) mode able to measure the SSH slope in the cross-track direction (Francis et al, 2007) as illustrated by Figure 2. In this paper, the cross-track slope (CTS) is given in micro-radians: a 1 μrad slope is approximately equal to a SSH gradient of 1 cm for 10 km, or a geostrophic current of 10 cm/s at mid-latitudes.

In this paper we use idealized OI simulations to explore the potential of the CTS derived from CryoSat-2's SARin mode to increase the resolution of mesoscale fields in the cross-track direction (methodology introduced in section 3). Our approach is to look at SARin technology in optimal conditions in section 4 and then to discuss what can be done in practice with current and future datasets in section 5.

3 Methodology

3.1 Overview

Le Traon and Dibarboure (2002, 2004), Chelton et al (2003) and Dibarboure et al (2011a) have shown that 2D SSH mapping is affected by many parameters (e.g. geometry, phasing or coordination of the constellation's orbits, high frequency ocean dynamics). To measure the potential of using a SARin slope to constrain mesoscale mapping we therefore use a simpler idealized 1D configuration.

We specifically focus on the cross-track direction (black segment from Figure 1) where the resolution is limited by the number of satellites in the constellation. In other words, this is a configuration where SARin slopes are ideal to complement lacking SSH measurements.

While performed for a given cross-track resolution (i.e. latitude), general conclusions can be derived from our analysis because correlation scales where shown to decrease with latitude as well (e.g. Jacobs et al 2001; Le Traon et al, 2003).

We measure the performance of mesoscale mapping using the following protocol:

- we simulate a mesoscale SSH "reality" profile, and we consider that the reality profile is in a frozen state, i.e. stationary over the 10-day period of a T/P or Jason repeat cycle (this strong assumption is discussed in section 5.3)
- the reality SSH field is sampled on measurement points to create error-free observations,
- errors are optionally added to the observations,
- observations are injected into a 1D optimal interpolator to create a "reconstructed" mesoscale field at the original resolution.

In this process, the statistical variance and correlation scales of the reality field are known analytically. Consequently the reconstruction is perfect if performed from enough error-free observations. In other words, differences between the reality and the reconstructed fields are the result of the omission or sampling error (not enough data to observe the signal) and commission or measurement error.

Note that, there is an additional error source in the mapping of real data: the imperfect modeling of signal and error covariances. This point is discussed in section 5.3.

3.2 Methodology

In this paper, we generate our reality H_{real} as a spatially correlated random Gaussian process (Equation 1). The default decorrelation scale is 150 km, i.e. consistent with findings from Le Traon et al (2003). In our first simulations (section 4.1), the oceanic variability used is 20 cm

RMS, i.e. we focus on zones of intense mesoscale activity (e.g. western boundary currents). Then we expand to different signal to error ratios in section 4.2. In section 5.3, we discuss the validity of the Gaussian methodology.

$$\mathbf{Corr(H,H) = exp\ (-x^2/d^2)} \qquad \textbf{Equation 1}$$

Our observation field H_{obs} is then constructed (Equation 2) by interpolating H_{real} at the desired resolution (30 km for an along-track simulation, 300 km for a cross-track simulation on a Jason-like orbit, and 100 km for a cross-track simulation on the CryoSat-2 orbit) and adding a white noise of 0.5 to 2 cm to the interpolated SSH values. This is arguably a pessimistic error level at 100+ km if compared with results from Dorandeu et al 2004, or Ablain et al 2011 : the noise they observe at a 7 km resolution would be reduced by along-track filtering of the SSH (factor of 2 for 30 km super-observations).

$$\mathbf{H_{obs}(x) = H_{real}(x) + \varepsilon(x)} \qquad \textbf{Equation 2}$$

Simulations shown in this paper do not include any along-track bias or long wavelength correlated errors as our sensitivity studies show no significant difference with noise-limited simulations. Although not shown in this paper, our simulated 1D mapping is degraded by correlated errors like operational mesoscale 2D mapping (e.g. Dibarboure et al, 2011c), but the anisotropy effect presented in section 3.3 and the impact of using SARin presented in section 3.5 are the same.

The reconstruction of the estimated mesoscale field H_{est} is performed with a 1D optimal interpolation derived from Bretherton et al (1976). H_{est} is obtained from Equation 3 where A is the matrix describing the covariance between H_{est} and H_{obs} of Equation 2, and C the matrix describing the covariance between the SSH observations (covariances are derived from Equation 1). The formal reconstruction covariance error matrix E is obtained from Equation

4, although in practice only its diagonal is used here (1-σ gray envelope around reconstructed SSH profiles).

$$H_{est} = A \,.\, C^{-1} \,.\, H_{obs} \qquad \text{Equation 3}$$

$$E = I - A \,.\, C^{-1} \,.\, A^{T} \qquad \text{Equation 4}$$

Many figures shown in this paper are limited to 3000 km segments for the sake of illustration but simulations were performed on very long profiles to ensure that the examples in this paper are representative of the statistical behavior of each configuration.

3.3 Observation anisotropy

Figure 3 shows one reality segment, sampled in the along-track direction (every 30 km) with 2 cm white noise added. The reconstructed field after optimal interpolation is almost identical to the reality field. The reconstruction error is 1.2 cm RMS i.e. 0.4% of the reality signal variance (18 cm RMS). Similarly, the along-track slope (bottom panel) is almost perfectly observed in the along-track direction.

Figure 4 shows the same reality segment, but positioned as a transect in the cross-track direction (black segment from Figure 1). In other words, each measurement (black dot) is the crossover between the transect and a different satellite track. In this figure, the SSH reality is sampled by a LRM altimeter every 300 km, i.e. the worst case configuration of a TP/Jason orbit. Because the Nyquist criterion is not met with a single satellite, many features are missed entirely in the reconstruction (e.g. at km #1000 or #1800 or #2200). The error reconstruction RMS is 46% of the signal variance. This figure illustrates the inability of a single satellite to observe large mesoscale, let alone features with radii smaller than 150 km.

Adding a second LRM altimeter (perfectly coordinated with the first one, i.e. like in the TOPEX/Jason tandem) significantly improves the resolution of the mesoscale field as shown by Figure 5. Although the Nyquist criterion is barely met, the reconstruction error is significantly reduced with an error of 8% of the signal variance. The error is consistent and slightly larger than the 5% obtained by Le Traon et Dibarboure (2002) because this segment represents the widest gap between roughly parallel tracks. These scenarios give the 1-LRM and 2-LRM reference configurations to which SARin experiments can be compared to infer the cross-track slope contribution in an ideal case.

The formal mapping error from Equation 4 is visible in each simulation as a grey envelope of vertical bars. This theoretical error is *–for these idealized simulations-* a very accurate statistical estimate of the error which could be made during the reconstruction process: the differences between the real (plain) and the reconstructed (dashed) SSH are consistent with the 1-σ boundaries defined with the grey envelope from Figure 3 and Figure 4.

The formal error represents the sum of the measurement error and the sampling error: it is as small as 2 cm near observation points (measurement noise) and as large as tens of centimeters at the center of the 300 km window between satellite tracks (sampling error). The anisotropy of the altimetry system is illustrated by the difference between the along-track and the cross-track formal errors. In the along-track direction (Figure 3) the error is always very small and dictated by the measurement error level whereas in the cross-track direction (Figure 4) the sampling error largely dominates between satellite tracks.

3.4 CryoSat-2's cross-track measurement

CryoSat-2 is ESA's ice mission (Francis, 2007). Equipped with an innovative radar altimeter (SIRAL – Synthetic Aperture Interferometric Radar Altimeter), and high-precision orbit determination (POD), CryoSat-2's primary objective is to serve Cryospheric science (Wingham et al, 2006). Cryosat's altimeter is operated almost continuously over ocean, mainly in LRM (i.e. conventional altimetry) or in the delay doppler / synthetic aperture radar

(SAR) mode which provides higher along-track resolution and lower noise level (Raney, 1998).

Furthermore, SIRAL also features a third mode: the SAR-interferometry (SARin) mode, which uses CryoSat-2’s two antennas (Francis, 2007). The combination of SAR and interferometry makes it possible to determine the cross-track slope of the surface from which the echoes are arriving. This is achieved by comparing the phase of one receive channel with respect to the other as first suggested by Jensen, 1999.

With the SARin mode, CryoSat-2 can provide one estimate of the local CTS every 0.05 seconds, in addition to the classical topography measurement (Figure 2). Moreover, the along-track resolution and the precision of the SSH is the same as for a LRM sensor (e.g. Jason-2). The resolution is 300 m in the along-track direction (synthetic footprint), and the slope is estimated from a cross-track footprint of the order of 7 km.

This unprecedented measurement was initially designed to be used over the margins of the Greenland and Antarctic ice sheets, where the surface slopes are steep. To that extent, SIRAL’s SARin mode was designed to have a cross-track slope accuracy of 200 µrad (Wingham et al 2006), but Galin et al (2012) reported a noise level of 20 µrad at a 7 km resolution and a bias of 8 µrad for 1000 km segments, using both detailed modeling of the finite radar resolution in range and angle, and the thermally driven behavior of the interferometer bench.

This should be compared to the typical mesoscale slope distribution in zones of intense mesoscale activity which ranges from 1 to 5 µrad at 150 km with values higher than 10 µrad on the edges of the largest eddies (observed on multi-satellite SSH maps from AVISO, 2010). Assuming that the long wavelength errors described by Galin et al (2012) are minimized with empirical cross-calibration mechanisms (discussed in section 5.2.1), and that the noise level is reduced by along-track filtering (discussed in section 5.2.2), it would become possible to use the SARin slope as a constraint for mesoscale mapping in the cross-track direction where LRM altimeters are blind.

Because the error level reported on CryoSat-2 is high with respect to the oceanic signal, our rationale is the following: we first look at the benefits of using error-free SARin CTS (section 4.1), then we perform sensitivity studies with respect to the ocean variability and measurement errors (section 4.2). From this background, we discuss the practical case of CryoSat-2 in section 5.

3.5 Improving the reconstruction with the cross-track slope

Figure 2 gives a qualitative illustration of how mesoscale mapping can exploit the SARin cross-track slope. Subplot (a) shows a 500 km along-track LRM profile with SSH only (simulated, error-free), whereas subplot (b) shows the information given by a SARin profile with SSH and cross-track slope. Both plots correspond to the reality from subplots (c) and (d).

From the SSH+CTS sample (subplot b), one can assume that the maximum value at -100 km is located on the right-hand side of the nadir track, that the minimum value at +150 km is probably near the nadir track, and that the maximum value at +400 km is located on the left-hand side of the nadir track. Adding a statistical description of mesoscale variability and slopes, it is possible to enhance the mapping in the cross-track resolution up to a distance equal to the spatial correlation radius.

This is achieved using a method derived from Le Traon and Hernandez (1992): we replace the SSH observation vector H_{obs} in Equation 3 by a vector composed of all observations (SSH and CTS), and we update matrixes A and C from Equation 3 and Equation 4 accordingly (see Appendix).

4 Results

4.1 Error-free simulations

In this section we infer what would be the optimal mesoscale improvement using SARin on a 300-km cross-track resolution (i.e. a Jason-like orbit). It is optimal for SARin in the sense that Le Traon and Dibarboure (2002, 2004) have shown that the main weakness of this orbit is the cross-track resolution, and it is the reason why TOPEX/Jason and Jason-1/Jason-2 were put in a spatially interleaved configuration. Thus we use this "reference orbit" and "reference tandem" to SARin-based simulations. We discuss the difference between this Jason-like configuration the (suboptimal) Cryosat orbit in section 5.1.

Adding the SARin slope constraint (error free) significantly improves the OI reconstruction as shown by Figure 6. This plot should be compared to Figure 4 where one LRM altimeter was barely able to recover 50% of the signal variance in the cross-track direction (Nyquist sampling not achieved). Thanks to local constraints on the SSH derivative, it is possible to recover features that were previously missed entirely (e.g. at km #1800 and #2200).

Quantitatively, on this example, the reconstruction error is only 6.96 cm RMS, i.e. 15% of the signal variance (vs. 50% for the LRM scenario on Figure 4). In other words, about 35% of the signal variance was recovered with the error-free slope. The 15% residual error should also be compared to the 8% of the configuration with two LRM altimeters (Figure 5): in this idealized simulation, a single SARin altimeter performs almost like two LRM altimeters.

Similarly, Figure 7 shows that a perfectly coordinated constellation of 2 SARin altimeters flying on a Jason-like orbit (150 km cross-track resolution) is able to properly reconstruct the SSH and slope reality fields even though the Nyquist criterion is barely met with SSH alone. Because slopes and covariance models add the constraint needed, the reconstruction error is only 1.83 cm RMS (i.e. 1% of the signal variance) and largely due to the error outlier of the first measurement and the 2 cm SSH measurement noise.

4.2 Sensitivity to signal to noise ratio

We performed a series of sensitivity tests on the slope error for 1 and 2 SAR-in altimeter constellations using very long simulations (2000 times the correlation radius). Figure 8 shows the RMS of the error reconstruction as a function of the standard deviation (STD) of the simulated SARin slope error (plain line). The 1-LRM and 2-LRM references are also given by the black dotted and dashed lines. Note that the observed error is consistent with the formal error given by Equation 4.

As expected, the reconstruction error decreases as the CTS error does, and the sigmoid shape on the logarithmic abscissa scale indicates that the largest gains are obtained between 1 and 5 µrad, i.e. near the peak of the cross-track slope probability density function.

The upper asymptotic value for slope errors higher than 20 µrad is 49%, i.e. the mapping error observed for 1 LRM sensor (dotted line). In other words, if the SARin error is large, it does not improve the reconstruction with the OI. Yet as expected from a theoretical point of view, this figure shows that even if the error STD of the CTS is 25 times larger than the SSH slope STD (i.e. factor of 600 in the covariance matrix), the OI never underperforms w.r.t to the 1-LRM scenario because untrustworthy observations are automatically downweighted by covariance matrix C.

If the OI covariance matrixes are properly set up, adding very noisy slope estimates (e.g. 10 to 20 µrad unmitigated error from Galin et al, 2012) can still improve the cross-track mapping, albeit in a very limited way.

The lower asymptotic value is 13% of the signal variance, i.e. only slightly larger than the 9% error observed with 2 LRM sensors (dashed line): using an error-free SARin instrument in an ideal configuration (1D, cross-track, 150 km radius for a 300 km sampling resolution) does not allow to fully reconstruct the signal, but a single SARin instrument yields results almost as good as two LRM sensors as per the example from Figure 5 and Figure 6. The residuals arise from sampling errors: although additional error-free parameters are used, there are still not enough measurements points to correctly resolve all mesoscale structures.

Results are similar for 2 x SARin simulations in Figure 9, even though the gain is more limited owing to the fact that 2 coordinated LRM altimeters already have a good sampling capability for 150 km radius features (Le Traon et Dibarboure, 2004). In this figure, the lower asymptotic value is 1.2%, i.e. very close to the 1% obtained with 4 coordinated LRM sensors: sampling errors would become marginal in a coordinated 2 x SARin configuration.

Because the variability of the cross-track slope is proportional to the variability of the SSH, we performed sensitivity studies to the latter (using constant correlation scales and SSH noise levels) to see how results from section 4.1 could be extrapolated out of intense mesoscale activity zones.

Figure 10 confirms that the reconstruction error is still sigmoid-shaped, and shifted along the abscissa axis as a function of the SSH variability. The breakthrough in mapping improvement is always achieved for slope error STD ranging from $0.5*\sigma_{slope}$ to $2*\sigma_{slope}$.

To be used globally in mesoscale mapping, SARin slopes would require an error level of the order of 0.1 to 0.5 µrad for mesoscale wavelengths. This is largely beyond what can be achieved with current data from Cryosat-2 (discussed in section 5.2).

5 Discussion: from theory to practice

5.1 Sensitivity to the satellite track geometry

The sampling pattern of the CryoSat-2 orbit (current SARin mission) and the Jason orbit (simulations from section 4) are very different. The latter has a 10-day repeat cycle (300 km cross-track resolution from Figure 1). In contrast, CryoSat-2 has a one-year repeat cycle with 3-day and 30-day sub-cycles, i.e. globally homogeneous sampling patterns with 1000 and 100 km cross-track resolutions respectively (Francis et al, 2007). CryoSat-2's orbit has no sub-cycle in the 10 to 20 day range associated with mesoscale temporal decorrelation (Jacobs et al, 2001).

As a result, for any 10 to 20 day period, CryoSat-2's measurements are aggregated in band-shaped patterns (100 km wide per 3-day sub-cycle) which are interleaved with band-shaped "blind spots" with no recent SSH observation (Figure 11). The impact on mesoscale observation in LRM mode is discussed by Dibarboure et al (2011c). As far as SARin slopes are concerned, there are two consequences of CryoSat-2's sampling pattern.

5.1.1 Track aggregation and data gaps

Firstly the SARin slopes located on the outer edges of the band-shaped aggregation of satellite tracks provide a unique capability to reduce the extent of the band-shaped blind spots by up to 2 * 150 km (one slope constraint on each side of the diamond not covered by CryoSat-2 tracks in Figure 11). This is useful to balance CryoSat-2's main sampling weakness when it comes to mesoscale observation.

Figure 12 illustrates this point: it shows the OI reconstruction for a 1500 km cross-track segment where CryoSat-2 measurements are aggregated in 100 km resolution bands where mesoscale features (150 km radius) are resolved, and interleaved with a 500 km wide blind spot where no CryoSat-2 track is available in the 15 day window corresponding the frozen field approximation.

The SARin-based reconstruction (subplot a) is slightly better because the outer edges are constrained by error-free slope estimates whereas the LRM-based reconstruction (subplot b) is not able to observe even a fraction of the large eddy at km #700 and the total reconstruction error is much higher (12.1 cm RMS vs. 6.7 cm RMS for SARin). Note that the overall improvement is limited to the outer edges of the large data gap (one decorrelation radius on each side) because the OI cannot "guess" the existence mesoscale structures if they are not remotely observed.

5.1.2 Orbit sampling differences

The second consequence of CryoSat-2's sampling pattern is the cross-track resolution *within* the track aggregations. CryoSat-2's sampling "bands" have a cross-track resolution of 100 km, i.e. more favourable to the observation of 150 km radius mesoscale features, albeit in limited areas. In this context, SARin data from Cryosat might be used to recover smaller mesoscale features (only within the satellite track aggregation).

Table 1 shows the mapping improvement (i.e. the reduction of cross-track reconstruction error) when the "reality" and OI correlation radiuses range from 50 to 150 km and for the Jason and CryoSat-2 orbits. All simulations were performed with a slope measurement noise of 1 µrad. On the Jason orbit, the cross-track mapping is improved mainly for large mesoscale (18%) but not for short mesoscale (5%) because the SARin slope cannot balance the limited resolution of the Jason orbit. The opposite is observed for CryoSat-2 (in the aggregation bands) owing to its cross-track 100 km cross-track resolution: the improvement is limited for 100 km or more and the highest improvement is observed for a 50 km radius.

In other words, with the CryoSat orbit, the SARin slope is an asset to improve the cross-track observation of smaller mesoscale features (in the band-shaped aggregation of satellite tracks), something that would not be possible on a Jason orbit.

Yet higher wavenumber (K) mesoscale eddies also have a smaller amplitude (the SSH power spectrum decreases as a function of $K^{-11/3}$ in the SQG theory, as per Le Traon et al., 2008). Thus changing the correlation radius also induces a reduction of the SSH STD and a reduction of the CTS STD from 2 µrad to 1.5 µrad (Table 1). In other words, higher precision SARin slopes would be needed in CryoSat-2's sampling bands because the smaller signal of interest also has weaker slopes.

To that extent, and considering the error level discussed in section 5.2, the CryoSat-2 orbit is less attractive than a Jason-like resolution would be, because the gain with SARin is geographically limited and because the orbit is more demanding in terms of CTS error budget.

5.2 Slope error

The simulations from section 4.2 showed that the enhancement of cross-track mesoscale mapping was possible in favorable signal to ratio conditions. The expected benefit from actual Cryosat-2 data raises the question of the error level of current datasets. Yet the error spectrum of SARin data in a mesoscale context is not known. Indeed, SARin acquisition zones on ocean are small and/or limited in time. So it is not possible to get datasets that are large enough to observe correlated errors in space or in time. The study from Galin et al (2012) is the first to provide a CTS error estimate as a bias and noise error on ocean through a comparison with a geoid model.

5.2.1 Biases and long wavelength errors

Galin et al (2012) report biases of the order of 8 µrad on their 1000 km segments. It is not so much a true bias, as a long wavelength correlated error (e.g. orbital revolution) since they also observe a correlation with thermal conditions on the orbit (i.e. linear on 1000 km segments). Yet, in this paper, we are ignoring biases and long wavelength errors because we assume that they can be accounted for by multi-satellite cross-calibration.

Indeed, at the intersection of satellite tracks (e.g. CryoSat-2 x CryoSat-2 or CryoSat-2 x Jason-2) crossovers points provide a double measurement where the actual SSH anomaly signal is partially cancelled if the temporal distance between both measurements is short enough. It is thus possible to use this observation to detect and to mitigate spatially and temporally correlated signals.

Tai et al (1988) have used this approach to empirically reduce orbit errors on the SSH and Dibarboure et al (2011b) have demonstrated the feasibility of reducing the cross-track slope error for the wide-swath altimetry mission SWOT. So, in theory, the same method could be used to reduce CryoSat-2's SARin slope biases. The method would exploit crossover observations using a combination of the along-track and cross-track slope for SARin / SARin crossovers, and a projection of the along-track slope into the opposite along-track plane for SARin / LRM crossovers.

Alternatively, long wavelength errors (500 km or more) can be accounted for in the mapping process itself, with an approach derived from Ducet et al (2000). These techniques are used operationally to remove SSH biases and 1000 km errors before mesoscale mapping (Dibarboure et al, 2011a), including for datasets with limited coverage (e.g. ERS-2 after the loss of its on board recorders). The same method could be used in the geographically-limited SARin acquisition zones to cross-calibrate long-wavelength errors in the cross-track slope.

5.2.2 Noise and short scale errors

In the recovery of the cross-track slope, Galin et al (2012) also observe on average 20 µrad of speckle-related noise at 1 Hz or 7 km resolution. The slope is computed from a distance ranging from 1 km to 8 km depending on the retrieval algorithm (phase-difference at the first point of arrival VS. model fit) and significant wave height (SWH) conditions.

The spatial correlation of mesoscale slope makes along-track filtering possible (including with non linear filters to remove spurious slopes) if the error is speckle-related (i.e. no along-track correlation of the CTS error). If we assume that a simple running average is used to get one super-observation for a 150 km radius (admittedly a crude filtering), the resulting mesoscale slope precision would be less than 4 µrad with current slope retrieval algorithms.

Moreover, Galin et al investigate the origin of residual SARin slope outliers such as the influence of wind and so-called sigma0 blooms. Yet sigma0 blooms can be detected and edited out in pulse-limited LRM altimetry (Thibaut et al, 2010). We can therefore assume that the largest SARin slope outliers can be detected as well, thus decreasing the overall slope error RMS of a non-Gaussian slope error distribution.

With Cryosat-2 we can probably observe only large eddies (2-σ) in zones of intense mesoscale variability. Elsewhere, SARin slopes from Cryosat-2 can probably barely improve cross-track mesoscale mapping because the instrument was not designed for this application (insufficient signal to error ratio).

5.2.3 MSS and geoid errors

In this section, we discuss MSS model errors and their influence on SARin slope anomalies in the context of mesoscale mapping. Indeed, mesoscale mapping is based on sea level anomalies (SLA), not sea surface heights (Dibarboure et al, 2012) and the SLA is created as the difference of the measured SSH and a temporal reference or <SSH>. The orbit used by CryoSat-2 is geodetic (one-year repeat cycle, described in Francis et al, 2007) so gridded MSS or geoid models are used as a <SSH> reference. The same stands for CTS anomalies which are the difference of the CTS measurement and the cross-track gradient of the MSS model. Consequently any error in the models generates a CTS anomaly error (i.e. an additional CTS error in Figure 10).

Pavlis et al (2008) show that in favourable conditions along the well-known TOPEX/Poseidon tracks, they observe an error of 2 µrad at 1 Hz for EGM08. In a different context, Sandwell and Smith (2009) have shown through comparisons with shipboard gravity that the accuracy of altimetry-derived gridded gradients was of the order of a few µrad in zones of rugged seafloor topography. More recently, Schaeffer et al (2012) have shown that the gradient error of their MSS model (CNES/CLS2011) ranged from 1 µrad along charted tracks of repetitive altimetry mission to 5 µrad in areas covered only by geodetic altimetry missions. Moreover, Andersen & Rio (2011) and Dibarboure et al (2012) highlighted differences between independent MSS models that range from 1 to 3 cm with wavelengths ranging from 3 to hundreds of kilometers (a few µrad after along-track smoothing).

The MSS/geoid error is therefore quite significant in the error budget of a SARin CTS anomaly, since it would add up to noise estimates from section 5.2.2. That error alone would make error-free CTS measurements difficult to use except in zones of strong mesoscale activity.

5.2.4 Expected and possible improvements

Comparing the figures of merit from section 5.2 to the sensitivity studies from section 4.2 shows that the precision needed to improve cross-track mesoscale mapping in strong currents is at the limit of CryoSat-2's current observation capability.

However, one might expect some improvements in the future. The primary error sources were shown to be speckle-related measurement noise and the MSS reference models used to generate the slope anomaly.

Concerning the former, it might be technically possible to update onboard software to get SAR data from both receive chains on ocean, and to change acquisition rates in SARin mode, essentially yielding 4 times as many independent looks, and reducing the noise level. Moreover, the SAR and SARin retrieval algorithms are relatively young, especially in an oceanography context (CryoSat-2 is an ice mission), and Galin et al give some interesting outlook that might result in a better precision: filtering, and weighting of beams…

And concerning the latter, our error estimate are derived from *2008-2001* generation MSS models, which are not yet integrating new geodetic data from CryoSat-2, Jason-1 GM (geodetic phase), let alone from new and upcoming missions flying on uncharted tracks (e.g. Sentinel-3A and 3B, HY-2). It is likely that the current and future altimeter datasets will decrease the error level of the future reference models, and especially at short wavelengths.

Beyond CryoSat-2, our findings raise the question of a prospective SARin demonstrator optimized for oceanography (with synergies with other applications). In this context, the outlook is even more promising because additional changes could be considered: on the orbit, on the hardware, and reference surface models.

CryoSat-2's orbit was shown to be suboptimal for SARin usage in section 5.1 and a dedicated mission could use a different orbit such as the ones analyzed by Dibarboure et al (2012) for the geodetic phase of Jason-1.

Moreover, if a new instrument derived from SIRAL were used on a dedicated SARin demonstrator, various upgrades could be considered to increase the number of statistically independent looks and to decrease the speckle-related noise: antenna design and beam width, baseline length, pulse timing (e.g. continuous or interleaved mode VS SIRAL's burst mode)… However it is possible that the global mesoscale requirement from section 4.2 (precision of the order of 0.1 to 0.5 µrad) might remain challenging.

Lastly, in the context of *global* SARin acquisition with a sufficient precision, such a prospective mission would acquire east/west gradients which would help resolve the shortest wavelengths in MSS, geoid or bathymetry models since they are difficult to resolve with the current anisotropy of altimeter data (Sandwell et al,, 2011). In turn, this would further mitigate the errors from the <SSH> reference discussed in section 5.2.3.

5.3 Validity and limitations of this work

In this section we discuss some approximations made in this paper, and the validity and limitations of these factors as an outlook for future work: the Gaussian properties of our "reality", the perfect a priori knowledge used in the mapping process, the simple 1D mapping methodology used, and the lack of temporal variability.

- In section 3.2, our reality is a random Gaussian process with a decorrelation function consistent with scales reported by Le Traon et al (2003). In practice, our reality has a flat power spectrum density for long wavelengths and a cut-off for shorter wavelengths. In other words, we do not use the covariance model from operational mesoscale mapping (e.g. Ducet et al, 2010), but our covariance model and the associated variance-preserved power spectra are representative of a diversity of wavelengths, much like along-track filtered altimeter measurements.
- In the OI, we use a priori knowledge of the covariance of the signal (H_{real}) and the covariance of the error (ϵ) in matrices A and C from Equation 3. In this paper, we use the true analytical covariance model used to simulate our dataset (i.e. the covariance

model of our Gaussian reality), resulting in a non-existent mapping error for error-free measurements. However, in practice, we only have an approximate knowledge of the true ocean decorrelation model (e.g. Jacobs et al, 2001 or Le Traon et al 2003) and of the altimetry error, so the OI process is not perfect. The same stands for the CTS parameter, and the a priori knowledge of the SARin data error. This can be a significant implementation problem so our findings should be revisited with real data. More importantly, this point highlights that one must acquire a better understanding of the SARin error spectrum before such data can used in an OI.

- Lastly one should note that the frozen field assumption and the 1D analysis (cross-track direction) represent a best case configuration for SARin. In reality, mesoscale signals temporally decorrelate over ±15 to 20 days. Thus our results are optimistic because they do not take into account the high frequency dynamics that Le Traon and Dibarboure (2002) showed to be difficult to resolve with constellations with less than 4 altimeter missions. There is also a large panel of complex geometric configurations that vary with latitude. Consequently, because 1D results are encouraging, the findings of this paper should be extended to much more sophisticated 3D simulations (OI or ocean model assimilation), taking into account orbit sampling dynamics (measurements are not ubiquitous, nor regularly spaced out) and the temporal variability of the ocean (reality is not frozen).

6 Conclusion

CryoSat-2's SAR interferometry (SARin) mode has the unprecedented capability to measure the sea surface height slope in the cross-track direction. It is possible to use this parameter to constrain mesoscale mapping, and to improve the resolution in the cross-track direction where the traditional (LRM) radar altimetry is limited by the number of satellites in operations.

Idealized mapping simulations show that a single error-free SARin sensor on a Jason-like orbit has the potential to perform almost like two coordinated LRM instruments. Sensitivity studies show that the breakthrough in mapping improvement is achieved for slope errors between 1 and 5 µrad for 150 km macro-observations, in zones of intense mesoscale activity. A better slope precision of the order of 0.1 µrad would be needed for global usage and/or to resolve smaller features (radius < 100 km).

The precision needed to improve cross-track mesoscale mapping is probably at the limit of current SARin products from CryoSat-2 (and only after multi-satellite cross-calibration and along-track filtering) which might observe only the strongest slopes (2-σ) in very energetic areas. The proof of concept is more attractive if we extrapolate to future improvements of SARin processors and ancillary datasets (e.g. MSS) and to a prospective mission improving upon SIRAL hardware and CryoSat-2 processors.

While encouraging, these results are optimistic, because all simulations were performed on a frozen SSH field (ocean dynamics and high frequencies are not taken into account), and only in the cross-track direction (i.e. optimal for the SARin slope) and they should be extended to much more complex 3D studies, or with real data from CryoSat-2.

7 Acknowledgements

This work was co-funded by the MyOcean Project and CNES. The authors would like to thank Pr. Duncan Wingham from the University College London, and Dr. Robert Cullen from ESA/ESTEC, and Dr Laurent Phalippou from T.A.S for their help.

8 Appendix: CTS methodology

To use the cross-track slope in the OI process, we use the following covariance models to describe the relationship between the topography H and the slope S:

$$cov_{hh}(\tau) = K.e^{-\left(\frac{\tau}{d}\right)^2}$$ **Equation 5**

$$cov_{hs}(\tau) = -\frac{2\tau}{d^2}.K.e^{-\left(\frac{\tau}{d}\right)^2}$$ **Equation 6**

$$cov_{ss}(\tau) = K.\left(\frac{4\tau^2}{d^4} - \frac{2\tau}{d^2}\right).e^{-\left(\frac{\tau}{d}\right)^2}$$ **Equation 7**

To inverse the problem, we replace A and C and H_{obs} from Equation 3 (and Equation 4), by A', C' and H'_{obs}, where H'_{obs} is the new observation vector including topography and slope measurements as the sum of the true signal H_{real} or S_{real} and a random error ε_H and ε_S estimated on the across-track position vector x(i):

$$H'_{obs} = \begin{bmatrix} H_{real}\big(x(1)\big) + \varepsilon_H(x(1)) \\ \vdots \\ H_{real}\big(x(N)\big) + \varepsilon_H(x(N)) \\ \vdots \\ S_{real}\big(x(1)\big) + \varepsilon_S(x(1)) \\ \vdots \\ S_{real}\big(x(1)\big) + \varepsilon_S(x(N)) \end{bmatrix}$$ **Equation 8**

Matrix C' is the new covariance matrix taking into account both topography and slope estimates

Equation 9

$$C' = \begin{bmatrix} C_{hh} & C_{hs} \\ C_{hs} & C_{ss} \end{bmatrix}$$

where C_{hh}, C_{hs}, and C_{ss} are the three covariance matrixes for each couple of observation type, built as a function of the distance $d_{i,j} = | x(i) - x(j) |$ separating measurements points #i and #j.

$$C_{hh} = \begin{bmatrix} cov_{hh}(d_{1,1}) & \cdots & cov_{hh}(d_{1,N}) \\ \vdots & cov_{hh}(d_{i,j}) & \vdots \\ cov_{hh}(d_{N,1}) & \cdots & cov_{hh}(d_{N,N}) \end{bmatrix} \qquad \textbf{Equation 10}$$

$$C_{hs} = \begin{bmatrix} cov_{hs}(d_{1,1}) & \cdots & cov_{hs}(d_{1,N}) \\ \vdots & cov_{hs}(d_{i,j}) & \vdots \\ cov_{hs}(d_{N,1}) & \cdots & cov_{hs}(d_{N,N}) \end{bmatrix} \qquad \textbf{Equation 11}$$

$$C_{ss} = \begin{bmatrix} cov_{ss}(d_{1,1}) & \cdots & cov_{ss}(d_{1,N}) \\ \vdots & cov_{ss}(d_{i,j}) & \vdots \\ cov_{ss}(d_{N,1}) & \cdots & cov_{ss}(d_{N,N}) \end{bmatrix} \qquad \textbf{Equation 12}$$

When the inversion is optimal we also account for the uncorrelated error ε_H and ε_S in the diagonal of C_{hh}, C_{hs}, and C_{ss} (not shown).

Matrix A' describing the covariance between the topography we want to reconstruct H_{est} and the new observation vector H'_{obs} is created with the method used for C', but using the distance $d'_{i,j}$ between the position x(i) of our observation points and the position x'(i) our unknown grid points.

9 <u>References</u>

- Ablain. M, S.Philipps, N.Picot, E.Bronner (2010): Jason-2 global statistical assessment and cross-calibration with Jason-1. Marine Geodesy, volume 33 supplement 1, doi: 10.1080/01490419.2010.487805
- Andersen.O., Rio.M-H. (2011): On the accuracy of current mean sea surfaces models. Proceedings of the 2011 Ocean Surface Topography Science Team Meeting (San Diego). http://www.aviso.oceanobs.com/en/courses/sci-teams/ostst-2011/index.html
- AVISO (2010): SSALTO/DUACS User Handbook : (M)SLA and (M)ADT Near-Real Time and Delayed Time Products, CNES document SALP-MU-P-EA-21065-CLS, latest version available on AVISO website: http://www.aviso.oceanobs.com/en/data/tools/aviso-user-handbooks/index.html

- AVISO (2011): Cal/Val and cross-calibration annual reports : http://www.aviso.oceanobs.com/es/calval/systematic-calval/index.html
- Bretherton, F. P., Davis, R. E., and Fandry, C. B., (1976): A technique for objective analysis and design of oceanographic experiment applied to MODE-73. Deep-Sea Research, 23:559-582
- Chelton, D. B., and M. G. Schlax (2003): The accuracies of smoothed sea surface height fields constructed from tandem altimeter datasets. J. Atmos. Oceanic Technol., 20, 1276-1302, 2003.
- Chelton, D. B., M. G. Schlax, and R. M Samelson, 2011: Global observations of nonlinear mesoscale eddies. Prog. Oceanogr., 91, 167-216.
- Cullen.R., D.J. Wingham, P. Viau, C.R. Francis, C. Mavrocordatos (2007): ESA's CryoSat-2 Multimode Level 0 to Level1B science processors – Algorithm design and re-launch verification with ASIRAS. Proceedings of the ENVISAT 2007 Symposium
- Dussurget.R., Birol.F., Morrow.R., De Mey.P. (2011): Fine Resolution Altimetry Data for a Regional Application in the Bay of Biscay, Marine Geodesy, Vol. 34, Iss. 3-4, 2011
- Dibarboure.G., M-I.Pujol, F.Briol, PY.Le Traon, G.Larnicol, N.Picot, F.Mertz, M.Ablain (2011a): Jason-2 in DUACS: first tandem results and impact on processing and products. , Marine Geodesy, 34:3-4, 214-241. doi: 10.1080/01490419.2011.584826
- Dibarboure.G., Labroue.L., Ablain.M., Fjørtoft.R., Mallet.A., Lambin.J., Souyris.J.C. (2011b) : Empirical cross-calibration of coherent SWOT errors using external references and the altimetry constellation, Transactions on Geoscience and Remote Sensing (in press, 10.1109/TGRS.2011.2171976)
- Dibarboure.G., Renaudie.C., Pujol.M-I, Labroue.S., Picot.N. (2011c): A demonstration of the potential of CryoSat-2 to contribute to mesoscale observation. Advances in Space Research (in press). doi : 10.1016/j.asr.2011.07.002
- Dibarboure.G., P.Schaeffer, P.Escudier, M-I.Pujol, J.F.Legeais, Y.Faugère, R.Morrow, J.K.Willis, J.Lambin, J.P.Berthias, N.Picot (2012): Finding desirable orbit options for the "Extension of Life" phase of Jason-1. Marine Geodesy (In Press).
- Dorandeu. J., Ablain.M., Faugere.Y., Mertz.F., Soussi.B., Vincent.P (2004): Jason-1 global statistical evaluation and performance assessment: Calibration and cross-calibration results. Marine Geodesy, Vol. 27, Iss. 3-4, 2010, doi : 10.1080/01490410490889094
- Ducet, N., P.Y. Le Traon and G. Reverdin, (2000): Global high resolution mapping of ocean circulation from the combination of TOPEX/POSEIDON and ERS-1/2. Journal of Geophysical Research (Oceans), 105, C8, 19,477-19,498.
- Francis, C.R., (2007): "Mission and Data Description", CS-RP-ESA-SY-0059, issue 3. ESA document. http://esamultimedia.esa.int/docs/CryoSat-2/Mission_and_Data_Descrip.pdf
- Galin.N., Wingham.D., Cullen.R., Fornari.M., Smith.W. (2011a): Measurement of the cross-track slope of the marine geoid with SAR-interferometric altimeter. Presented at the 2011 Ocean Surface Topography Science Team meeting (San Diego, Oct 2011) http://depts.washington.edu/uwconf/ostst2011/agenda.html
- Galin.N., Wingham.D., Cullen.R., Fornari.M., Smith.W., Abdalla.S. (2012): Calibration of the CryoSat-2 Interferometer and Measurement of Cross-track Ocean Slope. Transactions on Geoscience and Remote Sensing (in press), doi: 10.1109/TGRS.2012.2200298
- Jacobs, G., C.Barron, R.Rhodes (2001): Mesoscale characteristics, Journal of Geophysical Research, VOL. 106, NO. C9, PP. 19,581-19,595, 2001
- Jensen, J. R. (2009): Angle measurement with a phase monopulse radar altimeter, IEEE Trans. Antennas. Propagation, vol. 47, pp. 715–724, 1999.

- Labroue.S., F.Boy, N.Picot, M.Urvoy, M.Ablain (2011b): First Quality Assessment of the CryoSat-2 Altimetric System over Ocean. Submitted to ASR special issue "Oceanography, Cryosphere, and Freshwater Flux to the Ocean”.
- Leben.R., LoDolce.G. (2011): The New CCAR “Eddy” Ocean Data Server. Proceedings of the 2011 Ocean Surface Topography Science Team Meeting (San Diego). http://www.aviso.oceanobs.com/en/courses/sci-teams/ostst-2011/index.html
- Leben.R., Born.G., Engebreth.B. (2002): Operational Altimeter Data Processing for Mesoscale Monitoring, Marine Geodesy, Vol. 25, Iss. 1-2, 2010
- Le Traon, P. Y., M. C. Rouquet, and C. Boissier (1990), Spatial Scales of Mesoscale Variability in the North Atlantic as Deduced From Geosat Data, J. Geophys. Res., 95(C11), 20,267–20,285, doi:10.1029/JC095iC11p20267.
- LeTraon, P. Y., and F. Hernandez, (1992): Mapping the oceanic mesoscale circulation: Validation of satellite altimetry using surface drifters. J. Atmos. Oceanic Technol., 9, 687–698.
- Le Traon, P. Y., and G. Dibarboure, (2002): Velocity Mapping Capabilities of Present and Future Altimeter Missions: The Role of High-Frequency Signals. J. Atmos. Oceanic Technol., 19, 2077–2087.
- Le Traon, P.Y., Faugère Y., Hernandez F., Dorandeu J., Mertz F. and M. Ablain, (2003). Can we merge GEOSAT Follow-On with TOPEX/POSEIDON and ERS-2 for an improved description of the ocean circulation ? Journal of Atmospheric and Oceanic Technology, 20, 889-895.
- Le Traon, P.Y. and G. Dibarboure, (2004). Illustration of the contribution of the tandem mission to mesoscale studies. Marine Geodesy, 27, 3-13.
- Le Traon P.Y., P. Klein, B.L. Hua and G. Dibarboure, (2008). Do altimeter data agree with interior or surface quasi-geostrophic theory. Journal of Physical Oceanography, Volume 38 (5) , 1137-1142.
- May, D., and J. Hawkins (1991), Impact of the Geosat Altimeter Wet Tropospheric Range Correction in the Greenland-Iceland-Norwegian Sea, J. Geophys. Res., 96(C4), 7237-7247.
- Pascual, A., Y. Faugère, G. Larnicol, P.-Y. Le Traon (2006). "Improved description of the ocean mesoscale variability by combining four satellites altimeters." Geophys Reseach Letters 33(doi:10.1029/2005GL024633).
- Pascual A., C. Boone, G Larnicol, P.Y. Le Traon (2008) On the quality of real time altimeter gridded fields: comparison with in situ data, Journal of Atmospheric and Oceanic Technology, in press.
- Pavlis.N, Holmes.S., Kenyon.S. and Factor.J. (2008), An Earth gravitational model to degree 2160: EGM 2008, Presented at EGU
- General Assembly 2008, Vienna, Austria, April 13–18, 2008. http://earth-info.nga.mil/GandG/wgs84/gravitymod/egm2008/index.html
- Phalippou, L.; L.Rey; P. de Chateau-Thierry (2001): Overview of the performances and tracking design of the SIRAL altimeter for the CryoSat-2 mission. Geoscience and Remote Sensing Symposium, 2001. IGARSS '01. IEEE 2001 International, (doi: 10.1109/IGARSS.2001.978261)
- Philipps.S., M.Ablain, H.Roinard, E. Bronner, N.Picot (2012): Jason–2 global error budget for time scales lower than 10 days, Presented at the 2012 Ocean Surface Topography Science Team Meeting (Venise). Available online: http://www.aviso.oceanobs.com/fileadmin/documents/OSTST/2012/Philipps_jason2_global_error.pdf
- Raney.R.K (1998): The Delay/Doppler Radar Altimeter, IEEE Transactions on Geoscience and Remote Sensing, Vol. 36, No. 5., 1578 - 1588 (doi: 10.1109/36.718861)

- Sandwell, D. T., and W. H. F. Smith (2009), Global marine gravity from retracked Geosat and ERS-1 altimetry: Ridge segmentation versus spreading rate, J. Geophys. Res., 114, B01411, doi:10.1029/2008JB006008.
- Sandwell, D.T, E.Garcia, W.H.F.Smith (2011): Improved marine gravity from CryoSat and Jason-1. Presented at the 2011 ocean surface topography science team meeting. http://www.aviso.oceanobs.com/fileadmin/documents/OSTST/2011/oral/02_Thursday/Splinter%202%20GEO/06_%20Sandwell.pdf
- Schaeffer.P., Y. Faugère, JF. Legeais, A. Ollivier (2012): The CNES_CLS11 Global Mean Sea Surface computed from 16 years of satellite altimeter data. Marine Geodesy (In Press)
- Stum, J., Sicard, P., Carrere, L., Lambin, J. (2011): Transations on Geoscience and Remote Sensing, Volume 49, Issue 9, Pages 3211 – 3224, doi: 10.1109/TGRS.2011.2104967.
- Tai, C.K. (1988), Geosat Crossover Analysis in the Tropical Pacific 1. Constrained Sinusoidal Crossover Adjustment, J. Geophys. Res., 93(C9), 10,621–10,629, doi:10.1029/JC093iC09p10621.
- Thibaut, P. , Poisson, J. C. , Bronner, E. and Picot, N.(2010) 'Relative Performance of the MLE3 and MLE4 Retracking Algorithms on Jason-2 Altimeter Waveforms', Marine Geodesy, 33: 1, 317 — 335
- Wingham D.J., L. Phalippou, C. Mavrocordatos, and D. Wallis (2004): "The mean echo and echo cross-product from a beam-forming, interferometric altimeter and their application to elevation measurement," IEEE Trans. Geosci. Remote Sens., vol. 42, no. 10, pp. 2305–2323, Oct. 2004.
- Wingham D.J., C.R. Francis, S. Baker, C. Bouzinac, D. Brockley, R. Cullen, P. de Chateau-Thierry, S.W. Laxon, U. Mallow, C. Mavrocordatos, L. Phalippou, G. Ratier, L. Rey, F. Rostan, P. Viau and D.W. Wallis (2006): CryoSat-2: A mission to determine the fluctuations in Earth's land and marine ice. Advances in Space Research, Volume 37, Issue 4, 2006, Pages 841-871

10 Figure captions

Figure 1: 10-day sampling from an altimeter on the TOPEX/Jason orbit. The white segment highlights the along-track direction with one measurement every 7 km, and the black segment highlights the worst case configuration in the cross-track direction with one measurement every 315 km x cos(latitude).

Figure 2: Difference between LRM (a) and SARin (b) measurements in the optimal interpolation for common profiles of cross-track slope (c) and SSH (d). The SARin measurement allows to observe the cross-track slope in addition to the SSH profile given by the LRM mode.

Figure 3: Simulated Gaussian field (plain line), observation by a LRM altimeter in the along-track direction (dots, 30 km resolution), and reconstruction at each time step with an optimal interpolation (dashed line) with formal error estimates (grey bars). The upper figure shows the SSH (in cm), and the bottom panel the SSH slope (in µrad).

Figure 4: Simulated Gaussian field (plain line), observation by a LRM altimeter in the cross-track direction (dots, 300 km resolution), and reconstruction at each time step with an optimal interpolation (dashed line) with formal error estimates (grey bars). The upper figure shows the SSH (in cm), and the bottom panel the SSH slope (in µrad).

Figure 5: Simulated Gaussian field (plain line), observation by two LRM altimeters in the cross-track direction (dots, 150 km resolution), and reconstruction at each time step with an optimal interpolation (dashed line) with formal error estimates (grey bars). The upper figure shows the SSH (in cm), and the bottom panel the SSH slope (in µrad).

Figure 6: Simulated Gaussian field (plain line), observation by one SARin altimeter in the cross-track direction (dots couples, 300 km resolution), and reconstruction at each time step with an optimal interpolation (dashed line) with formal error estimates (grey bars). The upper figure shows the SSH (in cm), and the bottom panel the SSH slope (in µrad).

Figure 7: Simulated Gaussian field (plain line), observation by two SARin altimeters in the cross-track direction (dots couples, 300 km resolution), and reconstruction at each time step with an optimal interpolation (dashed line) with formal error estimates (grey bars). The upper figure shows the SSH (in cm), and the bottom panel the SSH slope (in µrad).

Figure 8: Cross-track reconstruction error (in % of signal variance) for one SARin altimeter as a function of the cross-track slope observation error (standard deviation in µrad). The black

dotted lines show the reconstruction error for one LRM altimeter and the black dashed line the reconstruction error for two LRM altimeters. The grey dashed line highlights the curve's point of inflection.

Figure 9: Cross-track reconstruction error (in % of signal variance) for two SARin altimeters as a function of the cross-track slope observation error (in µrad). The black dashed lines show the reconstruction error for two LRM altimeters and the black line the reconstruction error for four LRM altimeters. The grey dashed line highlights the curve's point of inflection.

Figure 10: Cross-track reconstruction error (in % of signal variance) for one SARin altimeter as a function of the cross-track slope observation error (in µrad) and for 3 levels of SSH variability.

Figure 11: CryoSat-2's sampling for 15 consecutive days. Satellite tracks (white lines) are aggregated in 500 km wide bands thanks to the 3 and 30 day sub-cycles, and interleaved with 500 km bands with few/no satellite tracks.

Figure 12: Simulated Gaussian field (plain line), observation in the cross-track direction (dots) by one SARin altimeter on the CryoSat-2 orbit (100 km resolution, packet-aggregated tracks), and reconstruction at each time step with an optimal interpolation (dashed line). Difference between SARin observation (top) and LRM observation (bottom) to constrain 1D OI reconstruction in the 500 km wide blind spot (grey rectangles).

Table 1: Reduction of the mapping error from LRM to SARin as a function of the simulation correlation radius. Unit: % of the signal variance. Right-hand side columns show the decreasing amplitude and slope of the eddy as a function of its radius (approximation of SQG theory).

11 Figures

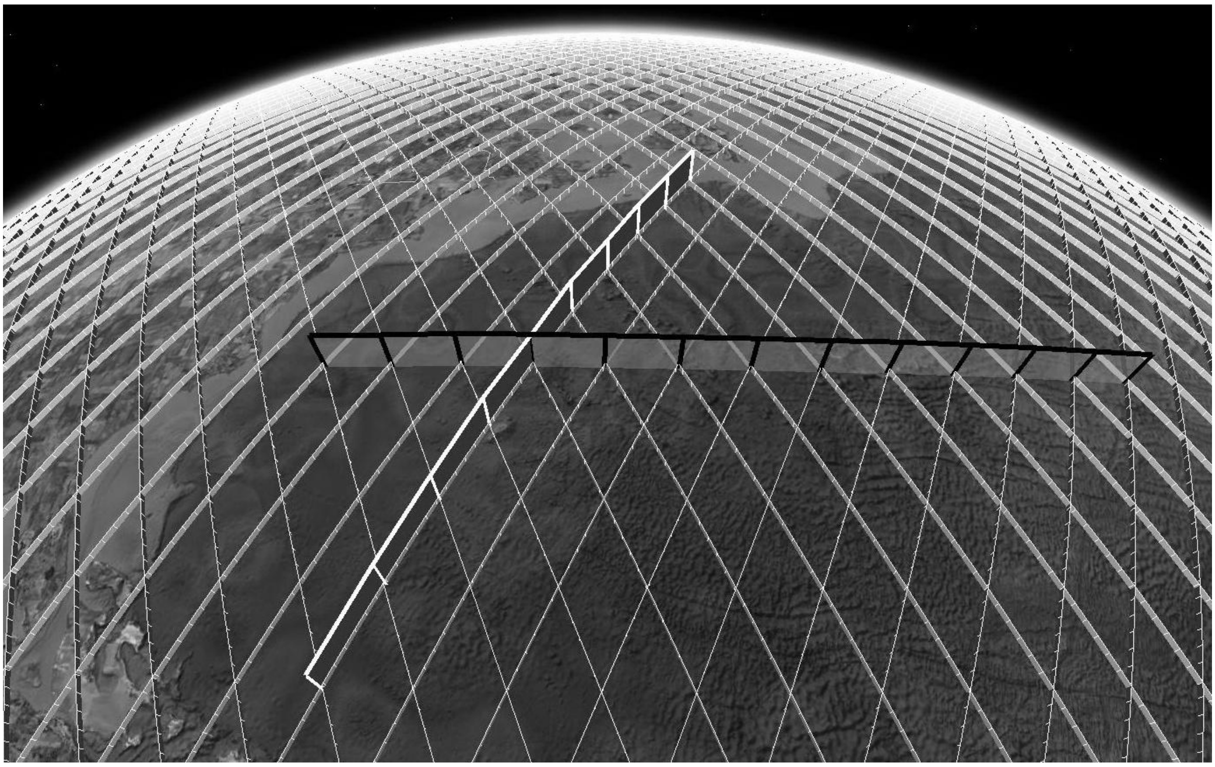

Figure 1 : 10-day sampling from an altimeter on the TOPEX/Jason orbit. The white segment highlights the along-track direction with one measurement every 7 km, and the black segment highlights the worst case configuration in the cross-track direction with one measurement every 315 km x cos(latitude).

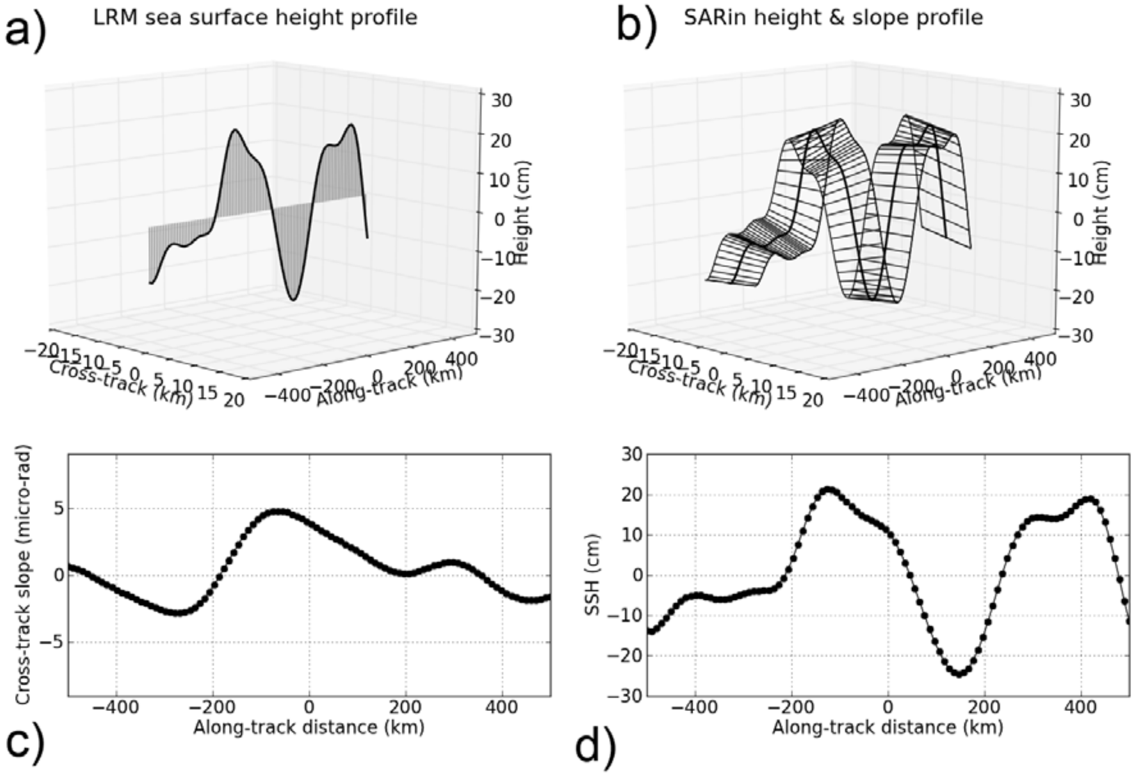

Figure 2 : Difference between LRM (a) and SARin (b) measurements in the optimal interpolation for common profiles of cross-track slope (c) and SSH (d). The SARin measurement allows to observe the cross-track slope in addition to the SSH profile given by the LRM mode.

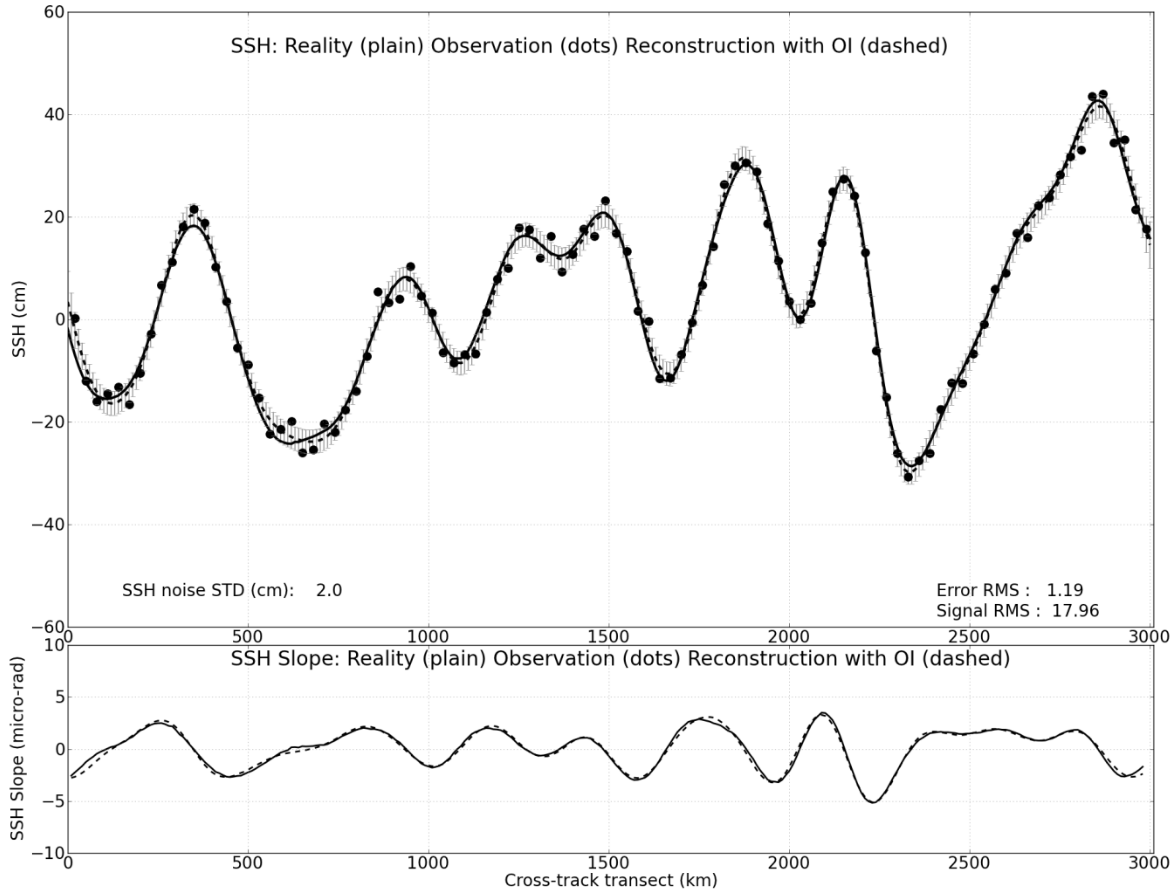

Figure 3 : Simulated Gaussian field (plain line), observation by a LRM altimeter in the <u>along-track</u> direction (dots, 30 km resolution), and reconstruction at each time step with an optimal interpolation (dashed line) with formal error estimates (grey bars). The upper figure shows the SSH (in cm), and the bottom panel the SSH slope (in µrad).

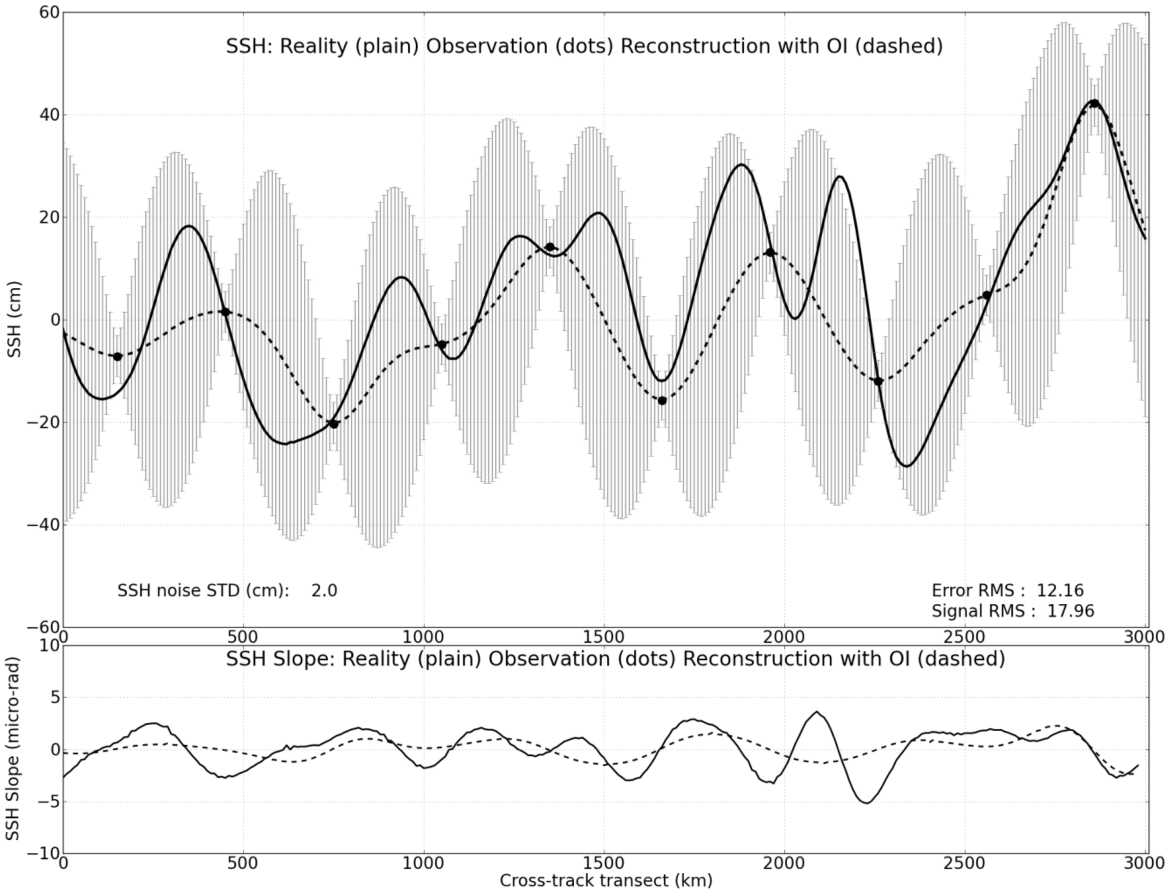

Figure 4 : Simulated Gaussian field (plain line), observation by a LRM altimeter in the <u>cross-track</u> direction (dots, 300 km resolution), and reconstruction at each time step with an optimal interpolation (dashed line) with formal error estimates (grey bars). The upper figure shows the SSH (in cm), and the bottom panel the SSH slope (in µrad).

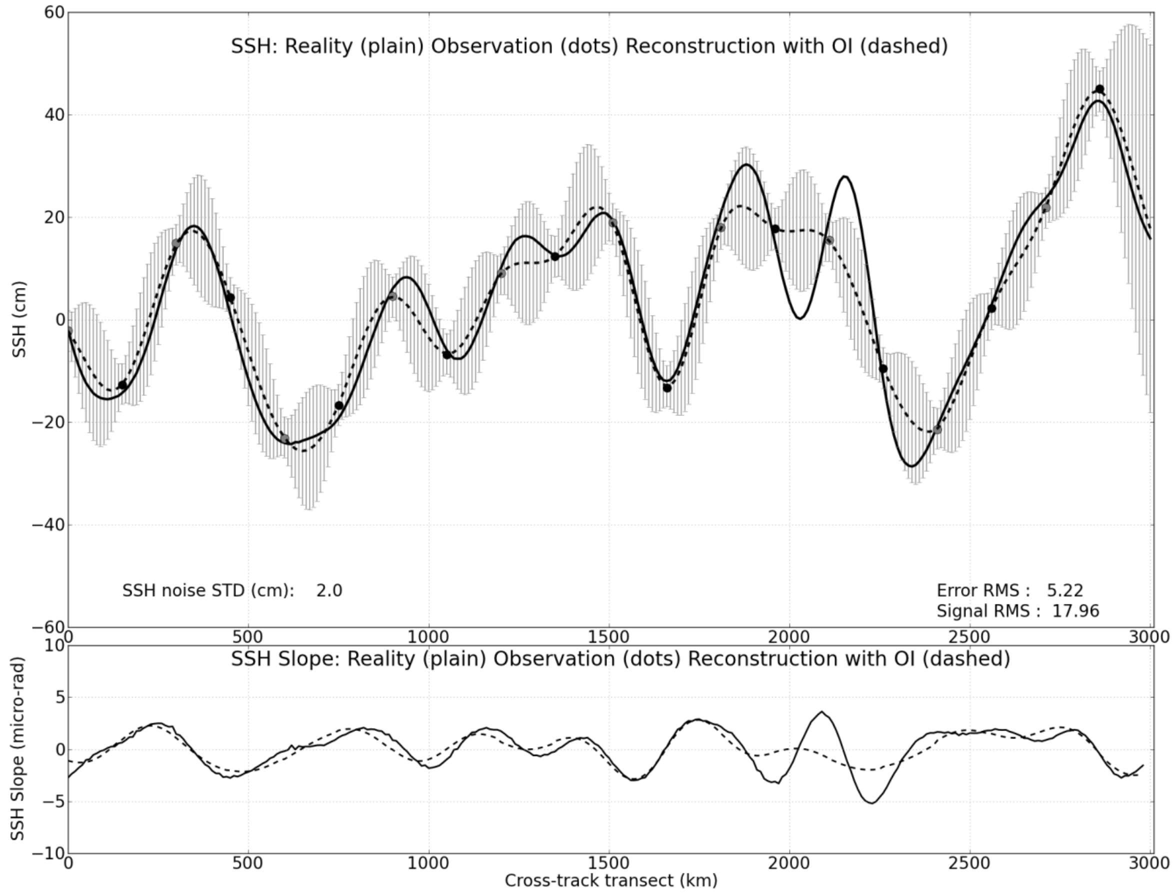

Figure 5 : Simulated Gaussian field (plain line), observation by <u>two LRM altimeters</u> in the cross-track direction (dots, 150 km resolution), and reconstruction at each time step with an optimal interpolation (dashed line) with formal error estimates (grey bars). The upper figure shows the SSH (in cm), and the bottom panel the SSH slope (in µrad).

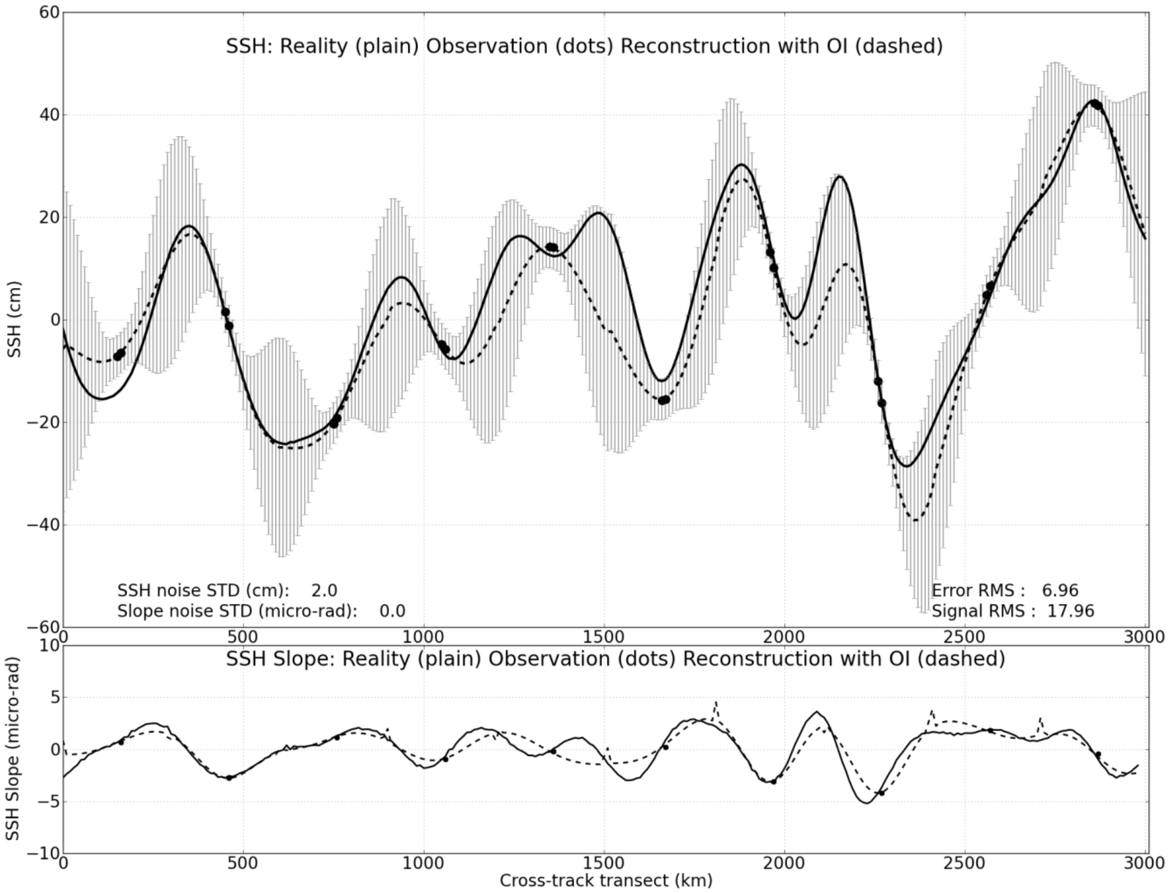

Figure 6 : Simulated Gaussian field (plain line), observation by <u>one SARin altimeter</u> in the cross-track direction (dots couples, 300 km resolution), and reconstruction at each time step with an optimal interpolation (dashed line) with formal error estimates (grey bars). The upper figure shows the SSH (in cm), and the bottom panel the SSH slope (in µrad).

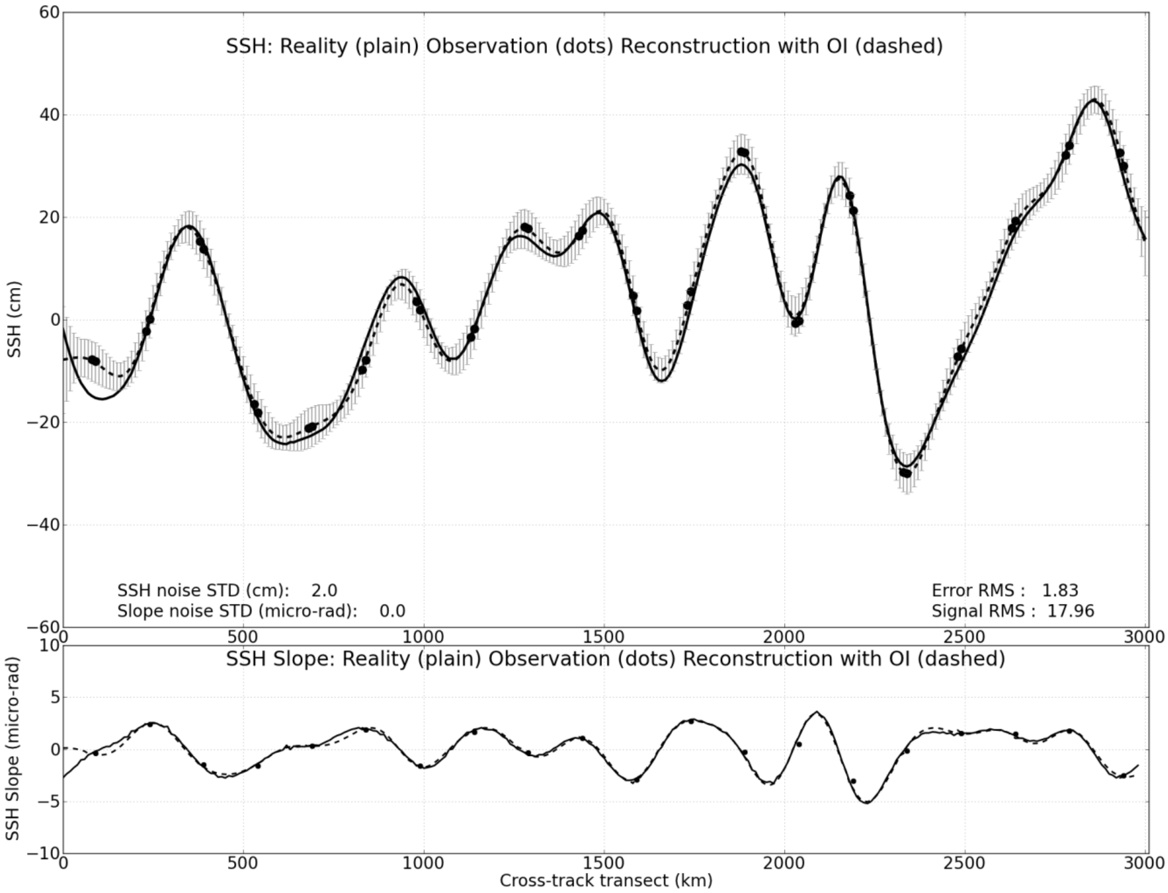

Figure 7 : Simulated Gaussian field (plain line), observation by <u>two SARin altimeters</u> in the cross-track direction (dots couples, 300 km resolution), and reconstruction at each time step with an optimal interpolation (dashed line) with formal error estimates (grey bars). The upper figure shows the SSH (in cm), and the bottom panel the SSH slope (in µrad).

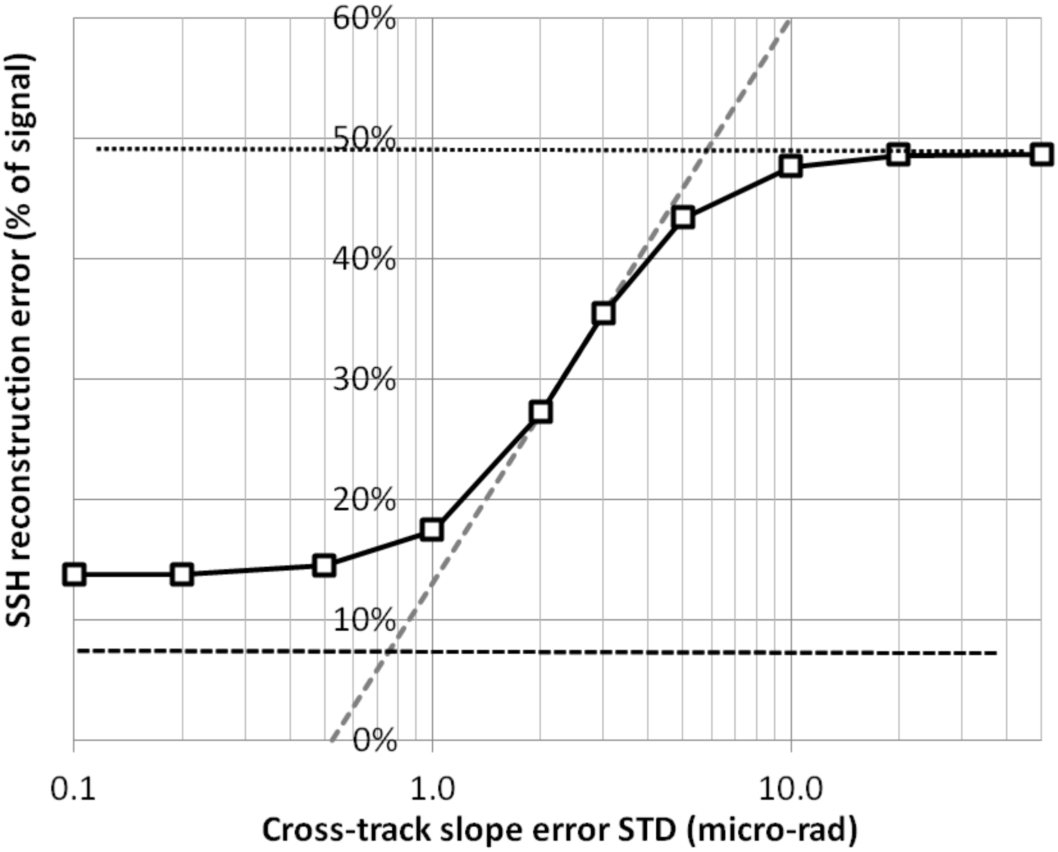

Figure 8 : Cross-track reconstruction error (in % of signal variance) for <u>one SARin altimeter</u> as a function of the cross-track slope observation error (standard deviation in µrad). The black dotted lines show the reconstruction error for one LRM altimeter and the black dashed line the reconstruction error for two LRM altimeters. The grey dashed line highlights the curve's point of inflection.

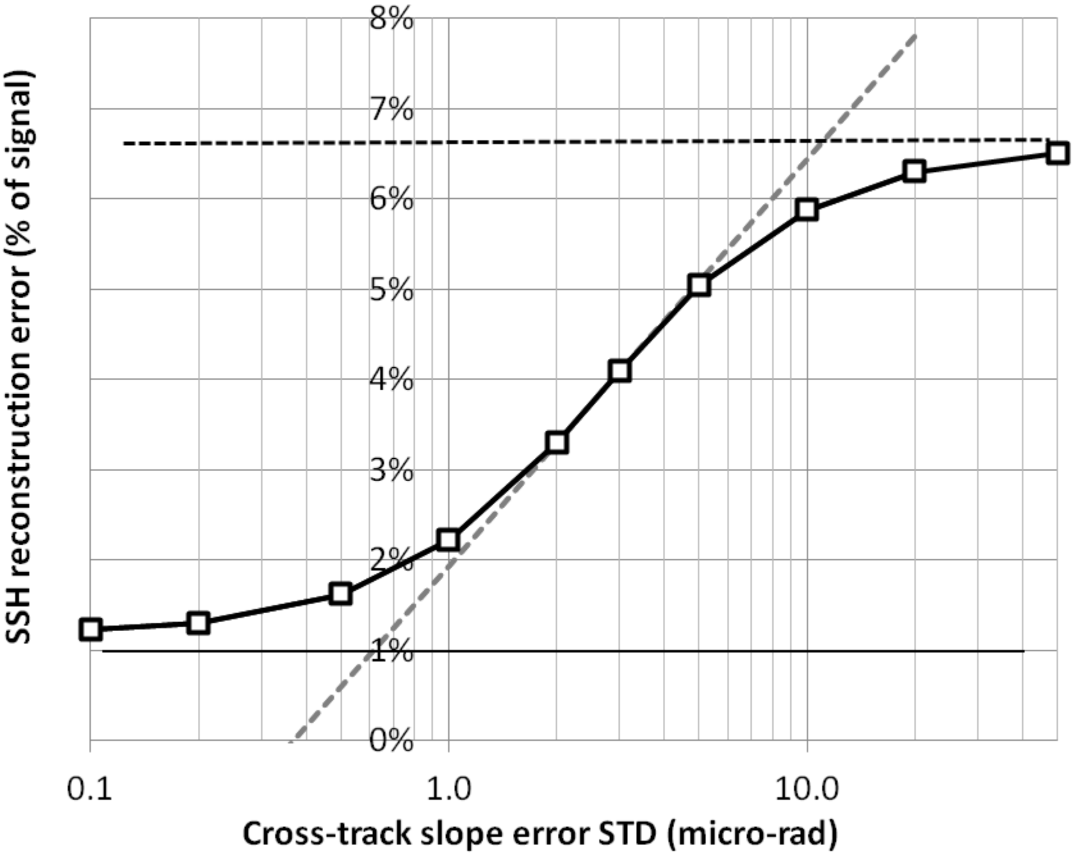

Figure 9 : Cross-track reconstruction error (in % of signal variance) for two SARin altimeters as a function of the cross-track slope observation error (in µrad). The black dashed lines show the reconstruction error for two LRM altimeters and the black line the reconstruction error for four LRM altimeters. The grey dashed line highlights the curve's point of inflection.

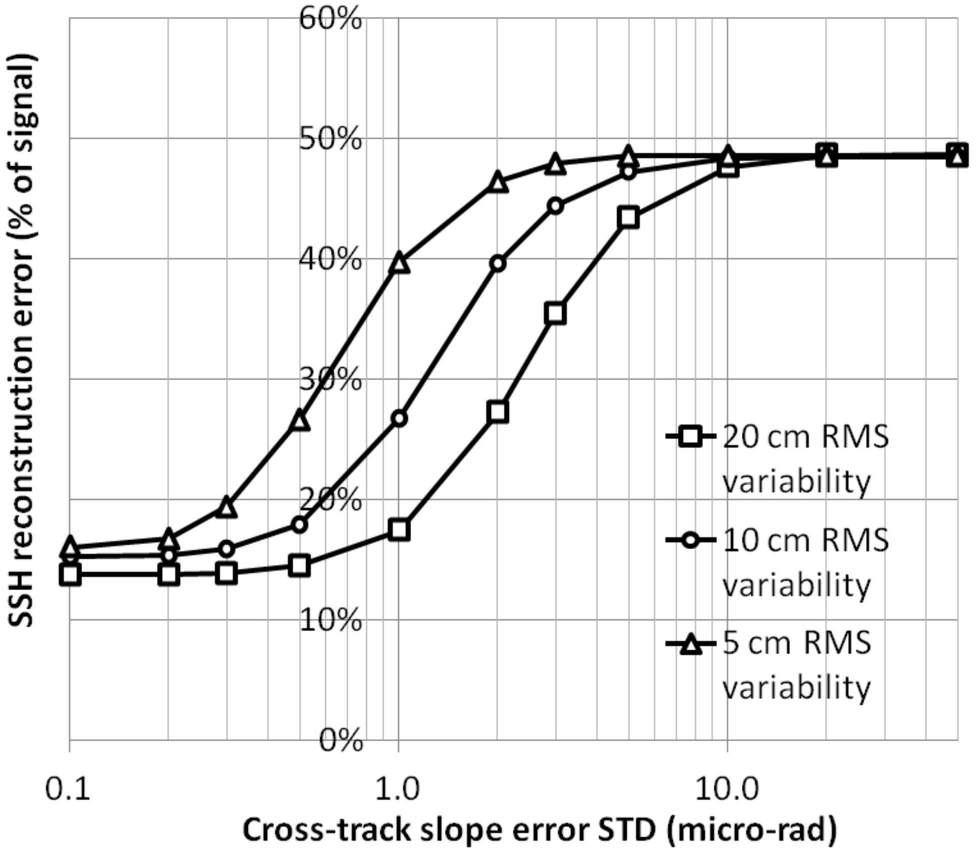

Figure 10 : Cross-track reconstruction error (in % of signal variance) for one SARin altimeter as a function of the cross-track slope observation error (in µrad) and for 3 levels of SSH variability.

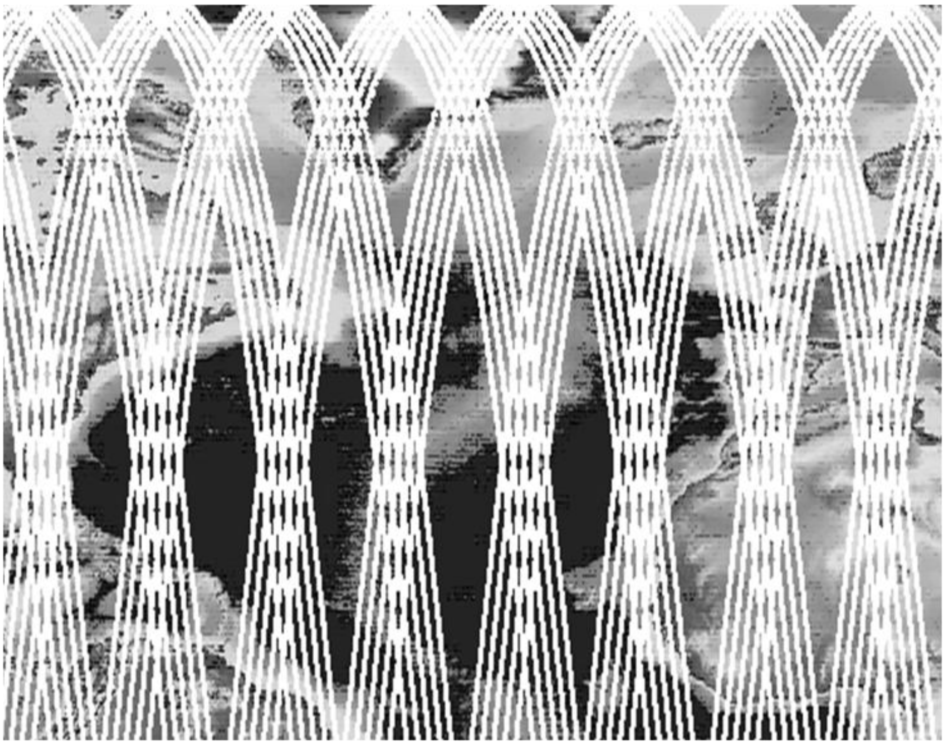

Figure 11 : CryoSat-2's sampling for 15 consecutive days. Satellite tracks (white lines) are aggregated in 500 km wide bands thanks to the 3 and 30 day sub-cycles, and interleaved with 500 km bands with few/no satellite tracks.

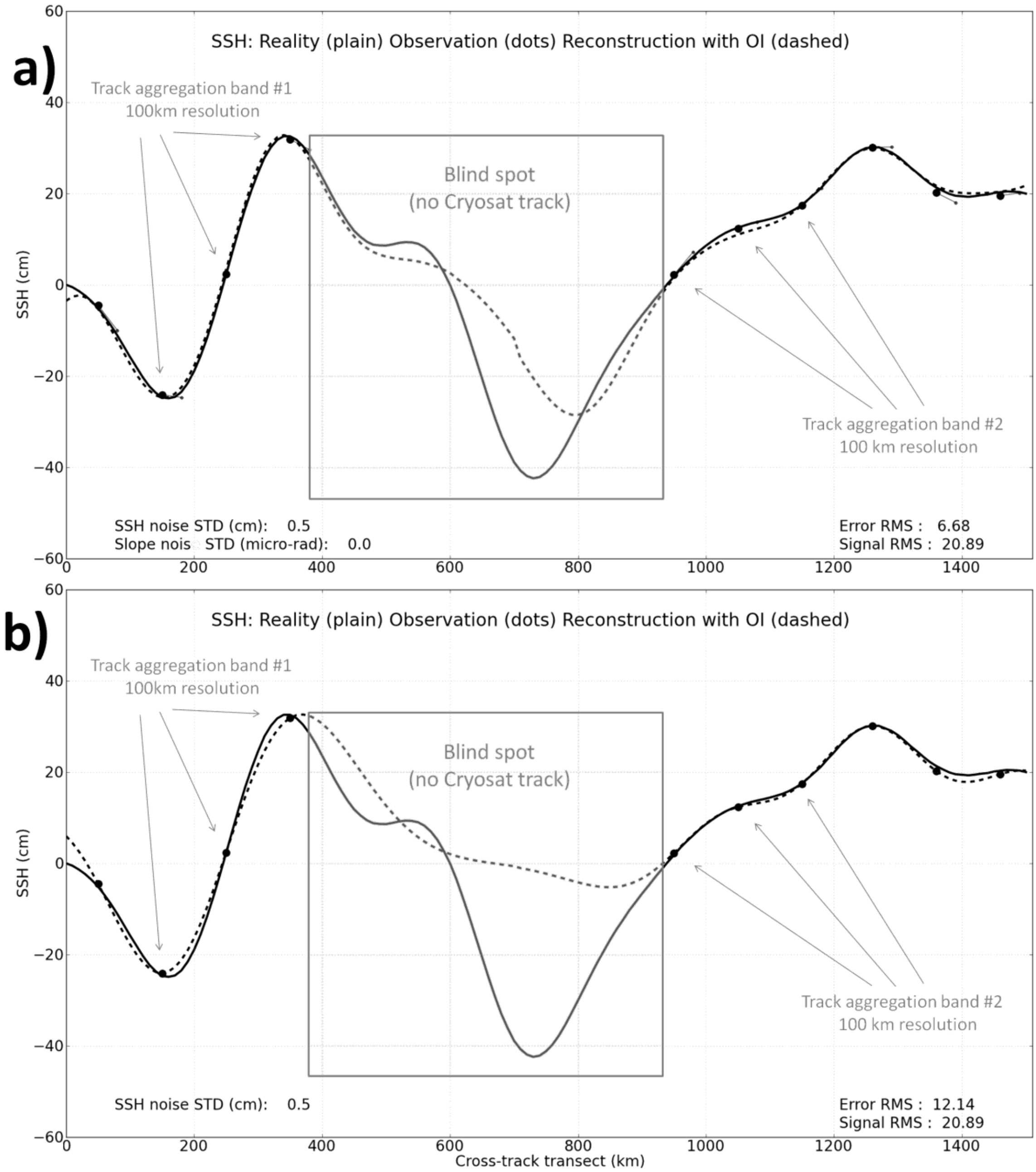

Figure 12 : Simulated Gaussian field (plain line), observation in the cross-track direction (dots) by one SARin altimeter <u>on the CryoSat-2 orbit</u> (100 km resolution, packet-aggregated tracks), and reconstruction at each time step with an optimal interpolation (dashed line). Difference between SARin observation (top) and LRM observation (bottom) to constrain 1D OI reconstruction in the 500 km wide blind spot (grey rectangles).

Radius	Mapping Improvement		Reality signal properties	
	Cryosat-2 Orbit	TP/Jason Orbit	SSH STD (cm)	SSH Slope STD (µrad)
150	0%	18%	20.0	1.9
125	1%	9%	15.8	1.8
100	2%	7%	11.8	1.7
75	8%	5%	8.1	1.5
50	14%	5%	4.8	1.4

Table 1: Reduction of the mapping error from LRM to SARin as a function of the simulation correlation radius. Unit: % of the signal variance. Right-hand side columns show the decreasing amplitude and slope of the eddy as a function of its radius (approximation of SQG theory).